EERI EARTHQUAKE SPECTRA

Seismic performance assessment of medical equipment using experimentally validated rolling and toppling nonlinear models

Jaime Guamán-Cabrera, M.EERI[1] ⓘD,
Juan Carlos de la Llera, M.EERI[2],
and Domingo Mery[3]

Abstract

During the last decades, several hospitals stopped service due to severe seismic damage to nonstructural components and medical equipment. This article investigates the dynamic behavior of medical equipment deployed in a full-scale, five-story building with two different support conditions, base isolated (BI) and fixed to the base (FB). Two nonlinear mathematical models, namely, rolling and toppling, are used to simulate the observed experimental responses using recorded data and the camera projection technique (CPT). CPT generated the possibility of measuring equipment horizontal displacements, slips, rotations, rocking, and toppling responses. The Euler–Lagrange formulation, along with the Stribeck friction model, was used to numerically model the rolling and in-plane rotation behavior of a four-wheel mobile cart (4WMC), which is considered to represent the trajectory of equipment supported on caster wheels. Besides, a simple two-dimensional (2D) rigid block model was used to describe the rocking and toppling behavior of locked and free-standing equipment. It was found that the 4WMC model was sensitive to the platform and wheels' initial orientation angles, as well as the static and kinetic friction coefficients. As it should be, the toppling model was sensitive to the block dimensions and the intensity of the shaking. It was concluded that both numerical models successfully predicted the equipment rolling, in-plane rotation, rocking, and toppling behavior, as long as neither severe lateral impacts nor significant changes in the equipment mass occur during the motion.

[1]Department of Structural and Geotechnical Engineering, Pontificia Universidad Catolica de Chile, Santiago, Chile
[2]Research Center for Integrated Disaster Risk Management (CIGIDEN) ANID/FONDAP/1522A0005, Macul, Santiago, Chile
[3]Computer Science Department, Pontificia Universidad Catolica de Chile, Santiago, Chile

Corresponding author:
Jaime Guamán-Cabrera, Department of Structural and Geotechnical Engineering, Pontificia Universidad Catolica de Chile, Av. Vicuña Mackenna 4860, Santiago Metropolitan Region 7820436, Chile.
Email: jwguaman@uc.cl

Introduction

Hospitals are complex systems of critical importance aimed to provide high responsiveness within communities, especially during disaster scenarios. They provide a wide range of specialized services using physical resources such as boxes in emergency rooms (ERs), operating rooms (ORs), and beds for conventional and intensive care units (ICUs). In turn, each of these rooms is equipped sometimes with sensitive, sophisticated, and expensive devices such as mechanical ventilators, ultrasound imagers, magnetic resonance imagings (MRIs), computed tomography (CT) scanners, and patient care beds among others (Hanson, 2009).

Nonstructural elements, systems, and contents (NSCs) commonly represent more than 90% of the total cost of a hospital building (Taghavi and Miranda, 2003). In addition, the continued operation of hospital critical rooms, which are typically impaired by NSC damage, is vital to preserve people's lives after earthquake-induced disasters (Lupoi et al., 2014; Myrtle et al., 2005; Simchen et al., 2004). Earlier investigations were able to describe the dynamics of contents through rigid body motion analogies based on observations, numerical analyses, or experimental tests (e.g. Aslam et al., 1978; Housner, 1963; Perry, 1881; Shenton and Jones, 1991; Yim et al., 1980). Other investigations have been able to include contact interface material and aspect ratio variability for rocking blocks (ElGawady et al., 2011). Similarly, Chatzis and Smyth (2012) modeled two-dimensional (2D) rigid rocking blocks considering the contact surface deformability as localized and distributed vertical springs and dampers. Recently, Wittich (2016) was able to assess not only the rocking, sliding, and twisting primary modes but also their interactions by performing several tests of a stiff steel tower with variable masses located at different heights. Lately, Bao and Konstantinidis (2020) investigated the dynamics of a 2D sliding-rocking block considering the impact with an adjacent wall, adopting that no free flight exists.

On the contrary, Fragiadakis and Diamantopoulos (2020) developed a comprehensive fragility assessment of free-standing rigid blocks located in a four-story reinforced concrete (RC) building. This study points out that the response of the structure and its contents are coupled and that the fragility of the contents should not be calculated independently of the building's damage progression. Likewise, D'Angela et al. (2021) performed fragility assessments of rocking components including different ground and floor motions, block geometries, intensity measures (IMs), and filtering phenomena of the building. This investigation concludes that more research on unanchored components is needed, including the interaction of diverse types of buildings.

Several investigations have tested real laboratory and hospital equipment, such as Konstantinidis and Makris (2008) who performed experimental tests and numerical simulations of refrigerators and incubators. Other researchers built small medical/laboratory enclosures supported by indoor shake tables and tested laboratory equipment placed on ceramic benches (Chaudhuri and Hutchinson, 2005); single and double window medical cabinets and desks (Cosenza et al., 2015; Di Sarno et al., 2015, 2019; Petrone et al., 2017) subjected to unidirectional and bidirectional input motions. Some of these studies provide

rocking and overturning fragility curves including equipment damage states with peak floor acceleration (PFA) and peak floor velocity (PFV) as IMs.

In addition, Nikfar and Konstantinidis (2017b) tested a heavy ultrasound supported on casters using vision-based motion tracking. This equipment was also tested for different orientations, and brake conditions, and included a medical cart in the experiments (Nikfar and Konstantinidis, 2017c). Later, Nikfar and Konstantinidis (2019) numerically simulated the response of the same pieces of equipment assuming they were located on the third floor of two buildings with different support conditions, that is, fixed to the base (FB) and base isolated (BI). These two latter studies presented fragility curves but without including their parameters. Recently, automatic hematology and coagulation analyzers, placed on a desk, have been tested on a uniaxial shake table to assess their sliding and toppling performances including the influence of adjacent walls and restrainers (Yu et al., 2023).

Moreover, full-scale experiments using large shake tables have been carried out to evaluate the performance of different NSCs deployed in full-scale, mid-rise steel and concrete buildings with different support conditions. For instance, Guzman Pujols and Ryan (2016) developed fragility curves that predict the level of disruption collectively achieved by office and hospital-like contents deployed in both two-story and five-story steel moment frame buildings, considering FB and BI systems. Similarly, Sato et al. (2011) present a comprehensive quantitative assessment of five medical appliances: an operation table, an electric laser machine, a heart–lung machine, a cardioverter defibrillator, and a ceiling pendant located on the third floor of a five-story RC building with three different support conditions, that is, FB and two distinct types of base isolation. In 2012, the University of California in San Diego (UCSD) conducted a full-scale experiment on a five-story RC building built on the NHER@UCSD Large High-Performance Outdoor Shake Table (Chen et al., 2013a). This building included a large variety of NSCs deployed at different floor levels, and it was tested under both FB and BI support conditions. The fourth level of the structure was intended to represent an ICU equipped with patient beds, patient lifters, and clinical gases, and the fifth level aimed to replicate an OR equipped with hospital freezers, medical cabinets, stretchers, and surgical lights (Chen et al., 2016). Hereafter this building will be referred to as the UCSD building.

Undoubtedly, research is progressing toward a better understanding of the NSCs dynamic behavior. Moreover, building construction codes and standards have recently provided general requirements and guidelines to include NSCs in the performance assessment of buildings. Nevertheless, neither ASCE/SEI 7-16 (American Society of Civil Engineers (ASCE), 2016) nor ASCE/SEI 7-22 (ASCE, 2022) have defined component-specific nonstructural performance objectives. Instead, only overall performance expectations are provided (National Institute of Standards and Technology (NIST), 2017). In addition, considerable damage to noncritical components and function loss are expected for design level earthquake (DLE) motions. Moreover, for lower ground motion intensities, neither these ground shaking intensities nor component performance expectations are explicitly defined (NIST, 2017).

To address this gap, this study investigates the seismic performance of some hospital equipment for small and strong ground motions. Herein, the UCSD test results are used due to their availability, reproducibility, and completeness. Therefore, this investigation builds on the data sources available at DesignSafe-CI (NEES-2009-0722 Project, Hutchinson et al., 2012), and on technical BNCS reports 1 through 4 (Chen et al., 2013a, 2013b; Pantoli et al., 2013a, 2013b). In addition, this study uses a method called Camera

Projection Technique (CPT) that estimates the 3D trajectory of a point captured in a video. This method consists of the following sequential procedures: (1) Camera Calibration (Hartley and Zisserman, 2004), (2) 3D Reconstruction (Faugeras, 1993), and (3) Tracking (Szeliski, 2022). Most of the camera videos of the medical equipment are publicly available on the DesignSafe-CI platform, and others were formally requested to Professor Tara Hutchinson (UCSD).

In section "Medical equipment description," this investigation describes the medical equipment deployed in levels 4 and 5 of the UCSD building. Section "Data collection and processing" briefly describes the data collection, processing, and includes the equipment frequency analysis from ambient vibrations. Section "Camera projection technique (CPT)" presents a detailed analysis using the CPT. In section "Mathematical model for rolling," a four-wheel mobile cart (4WMC) model, based on the Euler–Lagrange formulation, is used to predict the dynamic behavior of rolling equipment. In section "Mathematical model for toppling," a toppling model based on a 2D rigid block is proposed to characterize the equipment's rocking behavior. Both numerical models are then validated using analytical and experimental data. Section "Conclusions" presents the conclusions of this work.

Medical equipment description

Detailed information regarding the construction materials, seismic test protocol, and building structural response can be found in the BNCS reports 1 through 4. The UCSD building was subjected to 12 seismic inputs of different intensities and tested in the E-W (longitudinal) direction only. Table 1 (Appendix 1) lists the input motions considered in this study. As it was mentioned, the medical equipment was installed on the fourth and fifth building levels to reproduce an ICU and an OR, respectively. Figure 1 depicts the equipment arrangement, which allows rolling, in-plane rotation, sliding, rocking, and toppling. In the fourth level, the following unlocked equipment: ultrasound imager (UI3), mobile metal cart (MC2), and patient bed (PB2) were free to roll and rotate, whereas the locked patient bed (PB1) was free to slide, rock, and topple. Localized damage due to the impacts of UI3, PB2, and PS1 is also shown by the red stars. On the fifth floor, PS1 was free to roll and rotate, whereas the locked stretcher (PS2) and the free-standing wire shelving unit (WSU1) were free to slide, rock, and topple. The surgical light (SL) and the medical gas boom (MGB) hung from the sixth floor slab. It is important to mention that this study only considers equipment having the following support conditions: (1) free-standing, (2) locked swivel casters, and (3) unlocked swivel casters. Equipment with these support conditions may exhibit one or a combination of the above-described behaviors. Figure 2 shows the building, and the equipment included in this investigation. Table 2 (Appendix 1) summarizes the equipment support conditions, dimensions, and weights.

Data collection and processing

Data collection

The publicly available data of the NEES-2009-0722 project provides the structural, non-structural, and equipment raw accelerations (Hutchinson et al., 2012). Despite that most of the medical equipment was instrumented with accelerometers placed at the top of each unit, only E-W accelerations were registered. In addition, despite a large network video camera system was installed on each floor, no vision-based measurements were included in these tests.
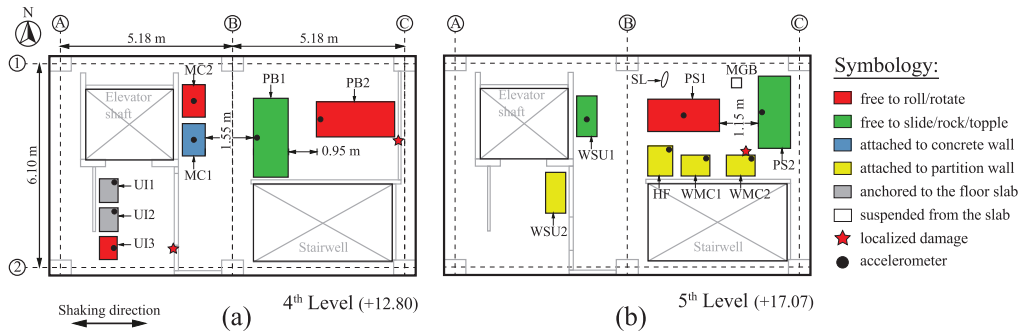
Figure 1. Medical equipment arrangement on the (a) fourth and (b) fifth building floor levels indicating their support conditions and the possibility of rolling, rotating, sliding, rocking, or toppling.

Figure 2. (a) UCSD building, (b) mobile metal carts (MC1, MC2), (c) wire shelving unit (WSU1), (d) ultrasound imagers (UI1, UI2 and UI3), (e) patient stretcher (PS1), and (f) patient medical beds (PB1, PB2).
Source: Photos courtesy of Professor Tara Hutchinson.

Building data processing

Building floor accelerations were reproduced following the methodology described in the BNCS Reports #2 and #3 for both BI and FB support conditions. The obtained building floor averaged accelerations, velocities, and displacements resulted very similar to those reported, with estimated differences of about ±5%.

Medical equipment data processing

A simple baseline correction was applied to the acceleration records by subtracting a cubic polynomial fit from the original record. In this case, no additional filter was applied to the
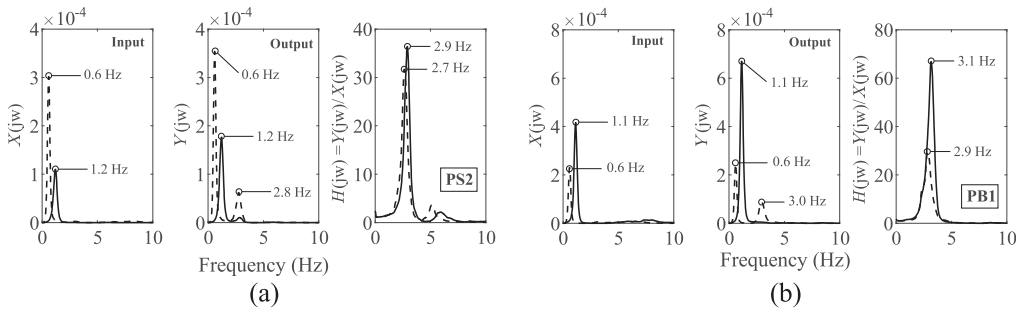
Figure 3. Transfer functions of: (a) stretcher (PS2), and (b) patient bed (PB1) including the identified fundamental frequencies during the DP + WN (before FB-1) and WN (before FB-6) tests.

baseline-corrected accelerations to keep the peaks unaltered. All equipment accelerations were synchronized in time with the building floor accelerations. Also, double pulse (DP) and low amplitude white noise (WN) results were used to identify the fundamental frequencies of the medical equipment. Figure 3 shows the Transfer Functions (H(jw)) of the stretcher PS2 and patient bed PB1 obtained using the signal processing toolbox of MATLAB (2018). Each plot includes the frequency response for the DP + WN test before the FB-1: CNP100 motion (solid line) and for the WN test before the FB-6: DEN100 motion (dashed line), respectively.

By observing the camera videos of these system identification tests, the rolling equipment exhibited rigid body motion, whereas the rocking equipment exhibited vibration and rocking motion for the lower (before FB-1) and strongest (before FB-6) tests, respectively. Table 3 (Appendix 1) summarizes the fundamental frequencies identified for each equipment considered in this study. Values show that the equipment having a rocking mode (PS2, PB1, and WSU1) experienced a smaller frequency variation as compared with that of the equipment having rolling behavior (UI3, PS1, MC2, and PB2). These frequencies were not close to the fundamental frequencies of the building system, which in average are 0.36 Hz (T = 2.8 sec.) and 1.00 Hz (T = 1.00 sec.), for the base-isolated and fixed-to-the-base conditions, respectively (Chen et al., 2016).

Camera Projection Technique (CPT)

Different sets of video cameras were installed in each story to track the movement of contents during both, BI and FB tests. Figure 4 shows the location of the IP and Coax cameras installed in the fourth and fifth stories. Despite the fact that a planned visual-based technique was not implemented, a CPT is used here to extract the dynamic equipment responses from the recorded videos. Herein, a central projection methodology is carried out where a mapping process from R^3 to R^2 is performed. During the mapping process, a camera ray will intersect a specific plane in space adopted as the image plane (Hartley and Zisserman, 2004).

The projection of a three-dimensional (3D) point (X, Y, Z) into a 2D point (u, v) of the image, as shown in Figure 5, can be expressed using the pinhole camera model with homogeneous coordinates (Hartley and Zisserman, 2004):
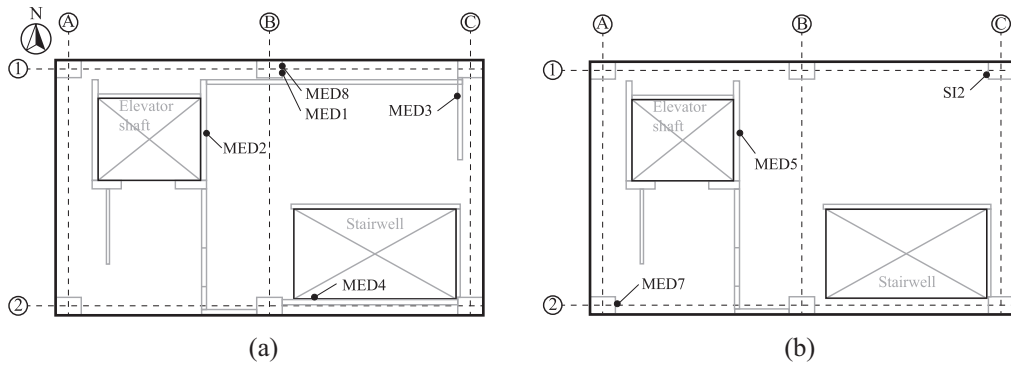
Figure 4. Location of video cameras installed at: (a) fourth story and (b) fifth story.
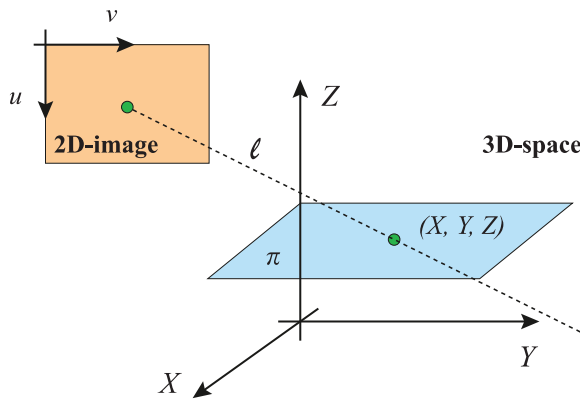

Figure 5. Geometric projection model.

$$\lambda \begin{bmatrix} u \\ v \\ 1 \end{bmatrix} = \begin{bmatrix} p_{11} & p_{12} & p_{13} & p_{14} \\ p_{21} & p_{22} & p_{23} & p_{24} \\ p_{31} & p_{32} & p_{33} & p_{34} \end{bmatrix} \begin{bmatrix} X \\ Y \\ Z \\ 1 \end{bmatrix} \tag{1}$$

where λ is a scale factor and p_{ij} are the elements of the 3×4 projection matrix $\mathbf{P}$. The estimation of the projection matrix is performed using a calibration approach (Hartley and Zisserman, 2004) with known corresponding pair points $(X_k, Y_k, Z_k) \leftrightarrow (u_k, v_k)$, for $k = 1, \ldots, n$, and $n \geqslant 8$. Typically, the 3D points are given in millimeters, and the 2D points in pixels. The calibration is an optimization method that estimates the matrix $\mathbf{P}$ by minimizing the following objective function:

$$J(\mathbf{P}) = \frac{1}{n} \sum_{k=1}^{n} \sqrt{(u_k - \hat{u}_k)^2 + (v_k - \hat{v}_k)^2} \rightarrow \min \tag{2}$$

where $(\hat{u}_k, \hat{v}_k)$ is the k-th projected point using Equation 1 and (X_k, Y_k, Z_k). An example is illustrated in Figure 6a. Using Equation 1 with the known projection matrix $\mathbf{P}$, it is possible to compute the 2D projection of any 3D point. However, the inverse is not true, and given the 2D representation and the matrix $\mathbf{P}$, it is not possible to determine the exact
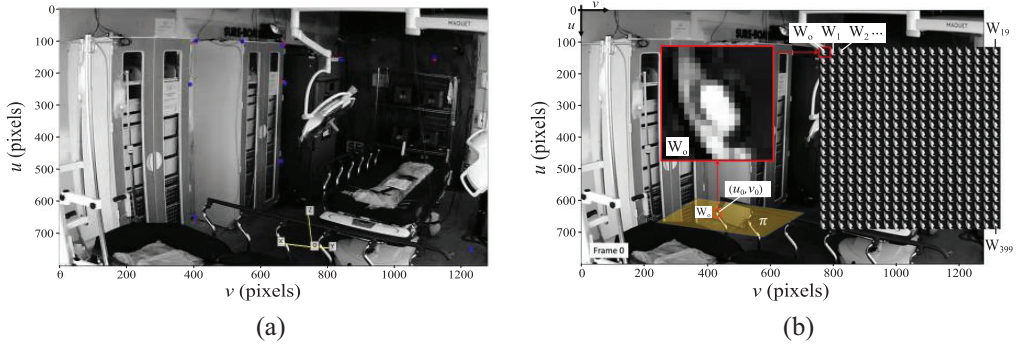
Figure 6. (a) Calibration points: in red are measured points (u_k, v_k) and in blue are modeled points $(\hat{u}_k, \hat{v}_k)$. (b) Tracking of a point centered in (u_0, v_0) and on plane π for the first 400 frames of the sequence.

location of a 3D point, since we only know the 3D line ℓ on which the 3D point lies (Figure 5). The exact location of the 3D point may be known with some extra information. Let us consider the plane π in the 3D space, on which the 3D point lies. This plane may be written as:

$$\pi : aX + bY + cZ + d = 0 \tag{3}$$

After manipulations of Equations 1 and 3, we obtain a system of three linear equations with three variables that can be easily solved for (X, Y, Z), since the parameters of the plane (a, b, c, d) and the elements p_{ij} of projection matrix **P** are known. The solution is:

$$\begin{bmatrix} X \\ Y \\ Z \end{bmatrix} = - \begin{bmatrix} p_{11} - p_{31}u & p_{12} - p_{32}u & p_{13} - p_{33}u \\ p_{21} - p_{31}v & p_{22} - p_{32}v & p_{23} - p_{33}v \\ a & b & c \end{bmatrix}^{-1} \begin{bmatrix} p_{14} - p_{34}u \\ p_{24} - p_{34}v \\ d \end{bmatrix} \tag{4}$$

To establish the 3D trajectory of a point in a 3D scene, we manually select a 2D point (u_0, v_0) on the first frame of the sequence (for $t = 0$) that lies on a known plane π in 3D space. This point is then tracked automatically across the next frames ($t > 0$) of the video. The point tracking in the video sequence is performed in three steps (Szeliski, 2022):

1. For $t = 0$ define a small window W_t centered in (u_t, v_t) and of size $m \times m$ pixels (in our case $m = 20$).
2. In the next frame, search for a window W_{t+1} of size $m \times m$ pixels in the neighborhood of (u_t, v_t) with the closest similarity to the window W_t, that is:

$$||W_t - W_{t+1}|| \rightarrow \min \tag{5}$$

3. Update (u_{t+1}, v_{t+1}) with the location of the center of W_{t+1} and repeat from step 2 using $t \leftarrow t + 1$ until the end of the sequence.

An example is shown in Figure 6b, where a point (u_0, v_0) is being tracked. Thus, for each estimated (u_t, v_t) in the trajectory, a 3D point (X_t, Y_t, Z_t) is calculated from Equation 4 assuming that all tracked points lie on plane π in 3D space.

Camera projection for rolling equipment

Following the CPT, the rolling displacements and in-plane rotation responses of the medical equipment located at the fourth and fifth floor levels were determined. These displacements and rotations are considered here to be experimental responses, and they will be later used to be compared with the results from the 4WMC numerical model. As an example, Figure 7 shows the CPT applied to the unlocked stretcher PS1 located at the fourth level and subjected to the BI-1: CNP100 motion. A script developed in Python was developed to read the selected 2D and 3D points on the frame, calibrate the camera, track the chosen moving points, and calculate the displacements in the X- and Y-directions.

First, all frames are extracted from each video, together with the width and height of the frames in pixels, the duration of the video, the number of frames, and the frame rate. Figure 7a displays the 2D fixed and moving points overlapped in the first frame. The 2D fixed points are arbitrarily selected within the scene; however, these points should be chosen in such a way that the following conditions are met: (1) their number should be equal to or greater than eight, (2) they should be traceable across all frames, (3) they should be evenly distributed within the scene, and (4) their 3D coordinates should be fully verifiable. Also, Figure 7a includes two moving points M1 and M2, which should be moving from frame to frame. Ideally, points M1 and M2 should be bright enough to ease the tracking process as shown in Figure 7b. Figure 7c shows the tracking of points M1 and M2 for 1,000 selected frames. Complete tracking of the moving points is crucial to fully characterize their displacements and rotations. Figure 7d shows the displacement traces of points M1 and M2, and as expected, both traces resulted very similar. Figure 7e shows the X- and Y-displacement orbits of M1 and M2, and the connecting twisted green lines indicate in-plane rotation. Finally, Figure 7f shows the extracted horizontal displacements versus the number of frames, which can be transformed into a time scale by using the frame rate of the camera.

Camera projection for rocking equipment

A similar procedure was used to obtain the rocking behavior of the locked stretcher PS2, locked patient bed PB1, and free-standing wire shelving unit WSU1. For instance, Figure 8a shows the stretcher PS2, captured from the camera SI2, including ten arbitrarily selected fixed points and two moving points M1 and M2 located on the stretcher side rails. In this case, this equipment was subjected to the FB-4: ICA100 motion, and consequently rocked over a YZ plane and finally toppled on its right side. Figure 8b depicts the moving point M1 being tracked in the first two frames. Figure 8c presents the tracking of M1 and M2 within the first 1,000 frames. Figure 8d displays the 3D displacement traces of M1 and M2. The connecting parallel green lines in Figure 8e indicate the rocking–toppling phenomenon. It is interesting to see that this technique is capable of disclosing the toppling phenomenon. Finally, Figure 8f presents an isometric view of the X, Y, and Z displacements in mm.
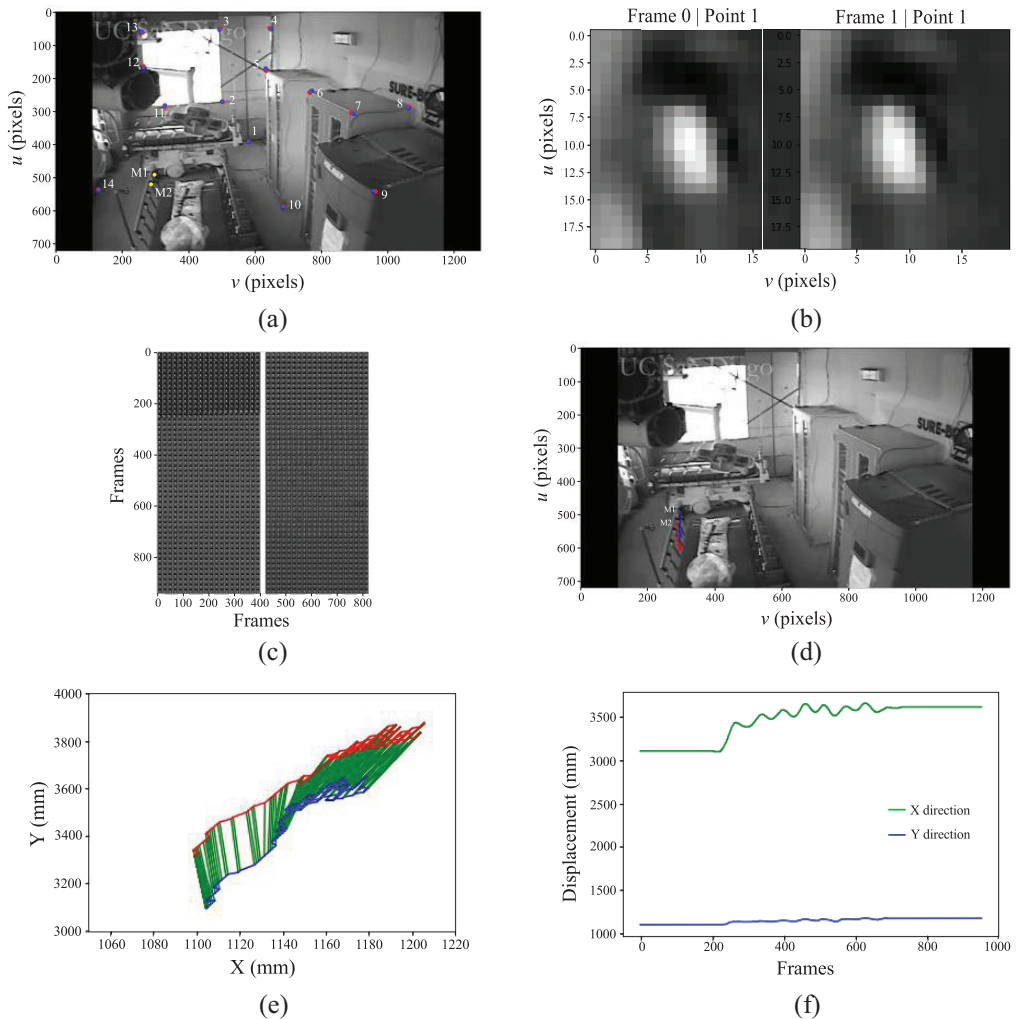
Figure 7. Camera projection of stretcher PS1: (a) 2D fixed and moving points overlapped in frame 0, (b) moving point M1 in frames 0 and 1, (c) frames showing the tracking of moving points M1 and M2, (d) horizontal displacement traces of moving points M1 and M2, (e) *X* versus *Y* displacement orbits, and (f) *X* and *Y* displacements versus number of frames.

Mathematical model for rolling

Four-wheel mobile cart model (4WMC)

A 4WMC rolling free on a horizontal surface is considered to represent the dynamic behavior of the medical equipment supported on unlocked swivel casters wheels. This model is based on the four-wheel-independent steering and four-wheel-independent driving (4WIS4WID) mobile robot model developed by Lee and Li (2015). Unlike the mechanisms normally found in wheel-mobile robots (Dhaouadi and Hatab, 2013; Lee and Li, 2015), the caster wheels of medical equipment are neither steering nor driving-independent, that is, the wheels are not auto-propelled, and they can adopt any orientation depending on the initial steering angle and the external forces applied. Moreover, the usual
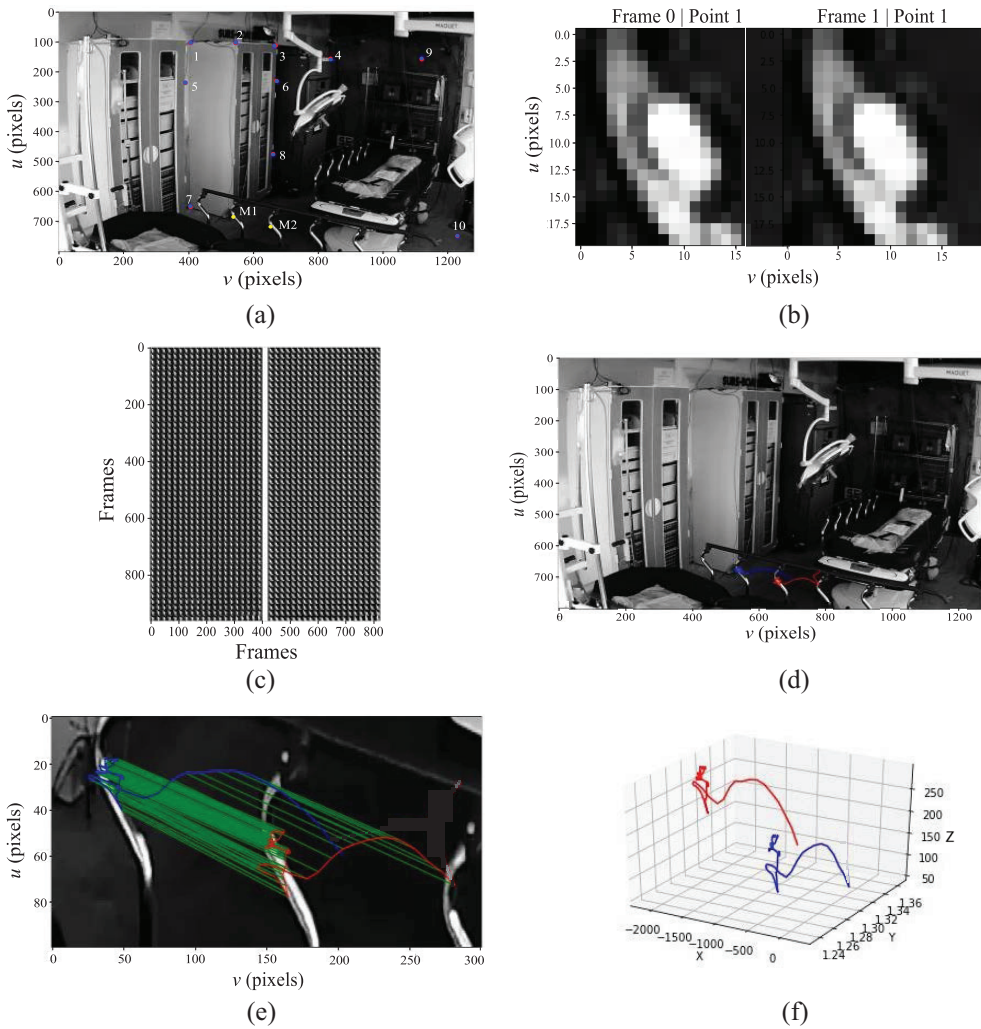
Figure 8. Camera projection of stretcher PS2: (a) 2D fixed and moving points overlapped in frame 0, (b) moving point M1 for frames 0 and 1, (c) frames showing the tracking of moving points M1 and M2, (d) 3D displacement traces of points M1 and M2, (e) 3D trajectory, and (f) X, Y, and Z displacements.

torque input forces generated by independent motors localized in each wheel are substituted herein by time-history horizontal floor accelerations. Another significant difference is the velocity-dependent friction (Stribeck) model adopted herein to characterize the contact friction between the wheels and the floor surface.

Figure 9 depicts the 4WMC model comprised of a rectangular platform and four caster wheels, free to displace in X- and Y-directions, and free to rotate around the vertical axis Z (yaw movement). At any time, the position and orientation of the platform are given by the coordinates of its geometric center (GC) X_P, Y_P, and the rotation angle θ. The position of each wheel is given by their coordinates x_i, y_i, and their steering angles δ_i. The velocities v_p and v_i represent the linear velocities of the platform and the wheels, respectively. The rolling velocities φ_i can be obtained after dividing the wheel linear velocities v_i by the wheel radius r, and ω_i represent the steering velocities of the wheels. It is important to
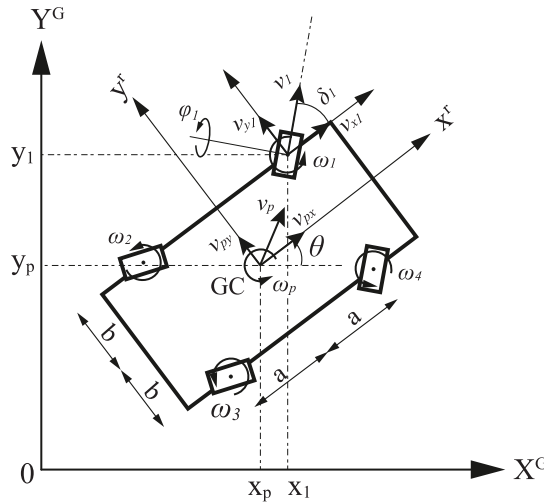
Figure 9. Schematic representation of a four-wheel mobile cart (4WMC).

mention that this model adopts the following assumptions: (1) the wheels are permanently in contact with the underlying floor surface, (2) no slip occurs between the wheels and the floor, (3) the position of the center of mass (CM) and the GC of the 4WMC are the same, and (4) all wheels have the same material properties and diameter.

Euler–Lagrange dynamic formulation. The Euler–Lagrange formulation is used herein to obtain the governing equations of motion of the 4WMC model. The Euler–Lagrange equation can be written as follows:

$$\frac{d}{dt}\left(\frac{\partial T}{\partial \dot{q}_i}\right) - \left(\frac{\partial T}{\partial q_i}\right) + \left(\frac{\partial V}{\partial q_i}\right) + Q_i^{(nc)} = Q_i^{(ext)} \qquad i = 1 : n \qquad (6)$$

where T and V are the kinetic and potential energy of the system, respectively, q and $\dot{q}$ are the generalized coordinates and velocities, respectively, and $Q_i^{(nc)}$ and $Q_i^{(ext)}$ represent the nonconservative and external generalized forces, respectively. For the 4WMC, the generalized coordinates, velocities, and accelerations are chosen as:

$$q = \begin{bmatrix} x_1 & x_2 & x_3 & x_4 & y_1 & y_2 & y_3 & y_4 & \theta & \delta_1 & \delta_2 & \delta_3 & \delta_4 \end{bmatrix}^T \qquad (7)$$

$$\dot{q} = \begin{bmatrix} \dot{x}_1 & \dot{x}_2 & \dot{x}_3 & \dot{x}_4 & \dot{y}_1 & \dot{y}_2 & \dot{y}_3 & \dot{y}_4 & \dot{\theta} & \dot{\delta}_1 & \dot{\delta}_2 & \dot{\delta}_3 & \dot{\delta}_4 \end{bmatrix}^T \qquad (8)$$

$$\ddot{q} = \begin{bmatrix} \ddot{x}_1 & \ddot{x}_2 & \ddot{x}_3 & \ddot{x}_4 & \ddot{y}_1 & \ddot{y}_2 & \ddot{y}_3 & \ddot{y}_4 & \ddot{\theta} & \ddot{\delta}_1 & \ddot{\delta}_2 & \ddot{\delta}_3 & \ddot{\delta}_4 \end{bmatrix}^T \qquad (9)$$

where x_i and y_i are the displacements of each wheel in x- and y-directions, respectively; θ is the in-plane rotation angle of the platform, and δ_i are the steering angles of each wheel. Similarly, $\dot{x}_i$, $\dot{y}_i$, $\dot{\theta}$, and $\dot{\delta}_i$ are the linear velocities of the wheels, angular velocity of the platform, and steering velocities of the wheels, respectively. Finally, $\ddot{x}_i$, $\ddot{y}_i$, $\ddot{\theta}$, and $\ddot{\delta}_i$ are the linear accelerations of the wheels, angular acceleration of the platform, and steering accelerations of the wheels, respectively. Considering the platform as a rigid body, the position vector r_w of each wheel w referred to a fixed system $\{X^G, Y^G\}$ can be written as:

$$r_w = r_p + Rr'_{w/p} \tag{10}$$

where r_p is the position vector of the GC of the platform; $r'_{w/p}$ is the vector $\overrightarrow{pw}$ with respect to the local system of the platform; and R is the corresponding rotation matrix. The kinetic energy T is obtained by:

$$T = \frac{1}{2}\dot{q}^T M_q \dot{q} \tag{11}$$

where $\dot{q}$ was already defined, and M_q is the generalized mass matrix of the system which can be expressed as $M_q = \sum J_i^T \hat{M}_i J_i$. Here, J_i denotes the Jacobian of the position vectors with respect to the displacement field q_i, and $\hat{M}_i$ is the individual mass matrix of the platform and the wheels.

Since the displacements and rotations of the 4WMC are restrained to the XY plane only, no gravitational potential energy is considered, and thus, $V = 0$ in Equation 6. The nonconservative friction forces developed in each wheel–floor interface are given by:

$$F_i = \begin{bmatrix} f_{\varphi_i} & f_{\delta_i} \end{bmatrix}^T \tag{12}$$

where f_{φ_i} and f_{δ_i} are the rolling and rotational friction forces of each wheel, respectively. As it was previously mentioned, the Stribeck friction model is adopted in this study. Thus, the friction coefficients can be written as (Nikfar and Konstantinidis, 2017a):

$$\mu(\dot{\varphi}_i) = \mu_{s\varphi} \operatorname{sech}(\beta\dot{\varphi}_i) + \mu_{k\varphi}[1 - \operatorname{sech}(\beta\dot{\varphi}_i)] + \gamma_n|\dot{\varphi}_i|^p \tag{13}$$

$$\mu(\dot{\delta}_i) = \mu_{s\delta} \operatorname{sech}(\beta\dot{\delta}_i) + \mu_{k\delta}\left[1 - \operatorname{sech}(\beta\dot{\delta}_i)\right] + \gamma_n|\dot{\delta}_i|^p \tag{14}$$

where $\mu(\dot{\varphi}_i)$ and $\mu(\dot{\delta}_i)$ are the rolling and rotational (steering) velocity-dependent contact friction coefficients, respectively; $\mu_{s\varphi}$ and $\mu_{s\delta}$ are the rolling and rotational static friction coefficients, respectively; $\mu_{k\varphi}$ and $\mu_{k\delta}$ are the rolling and rotational kinetic friction coefficients, respectively; $\dot{\varphi}_i$ and $\dot{\delta}_i$ are the rolling and rotational velocities, respectively; β is a parameter that defines the transition sharpness between the static and kinetic friction; γ_n is a viscous damping constant (slope of the Stribeck friction model); and p is a velocity exponent determined experimentally (Wolff and Constantinou, 2004). In this case, $p = 1$. The hyperbolic secant function $\operatorname{sech}(\cdot)$ allows for a continuous transition of the friction coefficient from zero to nonzero velocities (Xia, 2003). Thus, the friction forces in each wheel result:

$$f_{\varphi_i} = \mu(\dot{\varphi}_i)\operatorname{sign}(\dot{\varphi}_i)\left(m_w + \frac{m_p}{4}\right)g \tag{15}$$

$$f_{\delta_i} = \mu(\dot{\delta}_i)\operatorname{sign}(\dot{\delta}_i)\left(m_w + \frac{m_p}{4}\right)g \tag{16}$$

where $\mu(\dot{\varphi}_i)$, $\mu(\dot{\delta}_i)$, $\dot{\varphi}_i$, and $\dot{\delta}_i$ were already defined; m_w and m_p are the masses of each wheel and the platform, respectively; and g is the acceleration of gravity. The nonconservative friction force is then obtained as (Lee and Li, 2015):

$$Q^{(nc)} = \sum_{i=1}^{n} \boldsymbol{J}_i^T F_i \tag{17}$$

The seismic force vector is obtained by the following expression:

$$Q^{(ext)} = -\left(\sum_{i=1}^{n} m_i r_i(q)^T \right) \ddot{u}_f(t) \tag{18}$$

where m_i is the inertial mass, $r_i(q)^T$ is the Hessian matrix of the position vectors, and $\ddot{u}_f(t)$ is the floor horizontal acceleration vector applied in the desired direction. In this case, $\ddot{u}_f(t) = [\ddot{X}_f(t) \; \ddot{Y}_f(t) \; 0]^T$, where $\ddot{X}_f(t)$ and $\ddot{Y}_f(t)$ are the two time-history horizontal component floor accelerations. Equation 6 can be linearized to express the Euler–Lagrange equation in the form:

$$\bar{M}_i \ddot{q} + Q^{(nc)} = Q^{(ext)} \tag{19}$$

where $\bar{M}_i = M_{q|q=0}$, that is, the generalized mass matrix of the system evaluated at $q = 0$. Finally, after pre-multiplying all the terms in Equation 19 by $\bar{M}_i^{-1}$, the governing equations of motion of the 4WMC are obtained. To solve the system of equations, a state-space formulation was implemented in MATLAB (2018), using a fourth-order Runge–Kutta method as a numerical integrator with a time step of 1/10,000 sec.

Rolling model validation

To prove the reliability of the 4WMC numerical model, the horizontal displacement and in-plane rotation responses are compared to the experimental responses obtained from the CPT approach. The validation is carried out for the following unlocked equipment: (1) stretcher PS1, (2) patient bed PB2, (3) mobile metal cart MC2, and (4) ultrasound imager UI3. It is important to mention that in order to reproduce the experimental responses, the wheel's initial steering angle of each piece of equipment was taken into account. These initial angles were registered at the beginning and the end of each seismic test, as shown in Figure 10.

In Figure 11a through d, the top graphs show the building floor accelerations in X- and Y-directions, which are considered to be the input acceleration for each medical device. The middle graphs show the simulated X and Y horizontal displacement responses of the platform's CG overlapped with the experimental responses, and the bottom graphs display the numerical and observed platform in-plane rotations overlapped with the simulated caster wheel in-plane (steering) rotations.

Unlocked patient stretcher PS1. Figure 11a (middle) shows the predicted horizontal X (black dashed lines) and Y (gray dashed lines) displacements of the unlocked stretcher PS1 obtained by the 4WMC model and overlapped with the experimental responses (black and gray solid lines) obtained from the CPT. As can be observed, there is a very good match between the model and experimental results in both directions. Similarly, the predicted in-plane rotation θ of the platform (black dotted line), shown in Figure 11a (bottom), presents an excellent agreement with the experimental results (black solid line). Finally, the predicted steering rotation angle of each caster wheel is overlapped.

(a)   (b)

Figure 10. Wheel's initial and final position and orientation of: (a) patient bed PB2, and (b) stretcher PS1 during the seismic tests.
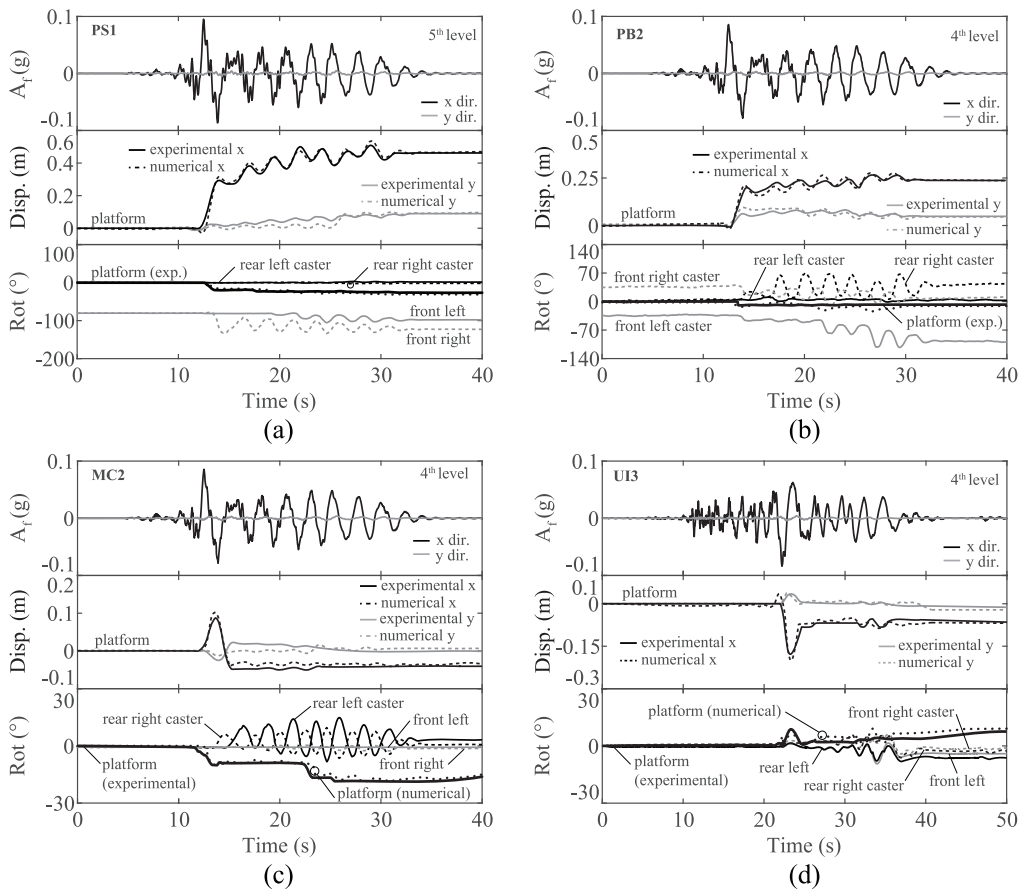Source: Photos courtesy of Professor Tara Hutchinson.

(a)   (b)

(c)   (d)

Figure 11. Floor input accelerations, predicted platform and wheels displacements and in-plane rotations overlapped with experimental responses of: (a) stretcher PS1, (b) patient bed PB2, and (c) mobile metal cart MC2 subjected to the BI-1: CNP100 motion. (d) Ultrasound imager UI3 subjected to the BI-2: LAC100 motion.

Unlocked patient bed PB2. Figure 11b (middle) displays the estimated horizontal X and Y displacements of the unlocked patient bed PB2 obtained by the numerical model and overlapped with the experimental responses obtained from the CPT. As before, there is an excellent agreement with the experimental results in both directions. The predicted in-plane rotation of the platform, shown in Figure 11b (bottom), results in a good match with the experimental rotation. In addition, the estimated caster wheel's steering rotation angles are included.

Unlocked mobile metal cart MC2. Figure 11c (middle) shows the predicted responses of the unlocked mobile metal cart MC2 obtained by numerical simulation overlapped with the experimental responses. Even though the match is not perfect, both displacement behaviors follow almost the same trend with very similar amplitudes. In Figure 11c (bottom), the estimated in-plane rotation history of the platform shows a very good match with that obtained in the experiment. In the same figure, the predicted steering rotation angle of each caster wheel is also shown. Note that, contrary to the trend observed in the wheels of PS1, the rear left and rear right wheels rotate in opposite directions, suggesting that this equipment is sensitive to experiencing the pivot steering effect (Hang and Chen, 2021). In fact, it was observed from the test videos that this equipment experienced in-plane rotations of about 180° and 100° during the FB-5 and FB-6 motions, respectively, and severely impacted the nearby patient bed PB1. Moreover, this equipment experienced a partial loss of its inertial mass during the FB-5: DEN67 motion after its shelves came out of place, and some water bottles were thrown away.

Unlocked ultrasound imager UI3. Figure 11d (middle) shows the estimated X and Y horizontal displacements of the unlocked ultrasound imager UI3 overlapped with the CPT responses. As before, there is an excellent agreement with the experimental results in both directions. Similarly, there is a close match between the analytical and experimental in-plane rotations of the platform as shown in Figure 11d (bottom). Despite that PB2 and MC2 are subjected to the same level of excitation, both devices responded differently, which confirms the model's ability to simulate different equipment behavior.

As we can see, the predicted displacement and rotation responses of the 4WMC model resulted very close to those obtained from the CPT. Nevertheless, due to the complex behavior of the rolling equipment, and the impacts observed during the last two (strongest) FB motions, the proposed analytical model should be used only in cases where the equipment neither experiences lateral impacts nor inertial mass variations. Consequently, the proposed 4WMC model is capable of predicting reasonable responses for the BI-1: CNP100 through BI-6: ICA140 motions and from FB-1: CNP100 through FB-4: ICA100 motions. Table 4 in Appendix 1 presents the model parameters used to obtain the responses shown in Figure 11. The dynamic interaction among different equipment and simulation of lateral impacts with inertial mass variation are beyond the scope of this study.

Mathematical model for toppling

2D toppling model

Figure 12 depicts trapezoidal (Giresini et al., 2016; Palmeri and Makris, 2008) and rectangular 2D rigid blocks considered to describe the dynamic behavior of the locked patient bed PB1, locked stretcher PS2, and the free-standing wire shelving unit WSU1. Herein,
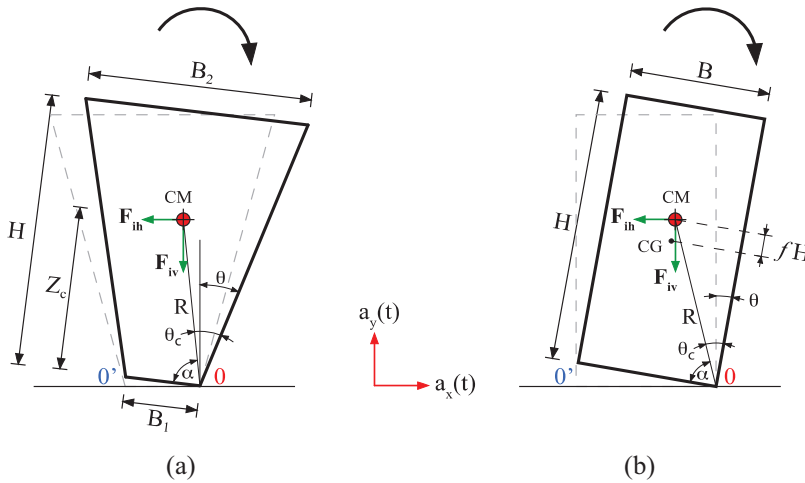
Figure 12. Schematic representation of the rocking motion of (a) trapezoidal and (b) rectangular free-standing rigid blocks under horizontal and vertical excitations.

the trapezoidal shape has been adopted for stretchers and beds because of their external dimensions, and because most of their masses are located at the mattress level.

Depending on the level of acceleration, geometric characteristics of the blocks, and location of their CMs, these blocks might move in unison with the floor without oscillation, they might be set into rocking motion, or they may topple. After the onset of rocking, the blocks will rotate about the out-of-plane axis going alternatively through points 0 and 0'. Generally, it is assumed that the static friction coefficient μ_s of the contact interface is large enough to prevent the blocks from sliding before engaging rocking movement. It is also assumed that the blocks shift from point 0 to 0' smoothly and without losing contact with the floor. The necessary conditions for these blocks to start rocking occur when the overturning moment produced by the horizontal inertia force F_{ih} exceeds the stabilizing moment exerted by the block weight W and the vertical inertia force F_{iv} (Yim et al., 1980). For the trapezoidal and rectangular blocks, these conditions are given by the following inequalities, respectively:

$$a_{xg} > \frac{0.5B_1}{Z_c} g \left(1 + \frac{a_{yg}}{g}\right) \tag{20}$$

$$a_{xg} > \frac{0.5B}{(0.5H + fH)} g \left(1 + \frac{a_{yg}}{g}\right) \tag{21}$$

where $a_{xg} = a_{xg}(t)$ and $a_{yg} = a_{yg}(t)$ are the horizontal and vertical floor acceleration time histories respectively; B_1 and Z_c are the short base of the trapezoid block, and the perpendicular distance from the short base to the CM, respectively; B and H are the width and height of the rectangular block, respectively; f is a percentage of the rectangular block height to account for the difference between the GC and the CM of the block; and g is the acceleration of gravity. Note that these inequalities are mass-independent. Once the rocking has been initiated, the governing equation of motion for both blocks can be expressed as (Makris and Roussos, 2000; Yim et al., 1980):

$$I_o\ddot{\theta} + mgR\sin(\theta_c\text{sign}[\theta] - \theta) + mR\sin(\theta_c\text{sign}[\theta] - \theta)a_{yg} = -mR\cos(\theta_c\text{sign}[\theta] - \theta)a_{xg} \quad (22)$$

where I_o is the rotational moment of inertia of the block about the pivot points 0 or 0';
$\theta = \theta(t)$ and $\ddot{\theta} = \ddot{\theta}(t)$ are the rotation (rocking) angle, and angular acceleration time histories, respectively; m is the mass of the block; R is the diagonal distance from either pivot point 0 or 0' to the block CM; θ_c is the critical rotation angle; and a_{xg}, a_{yg}, and g were already defined.

The conservation of momentum about point 0' between the moment just before pivoting on the left corner, and immediately after pivoting implies that (Yim et al., 1980):

$$I_o\dot{\theta}_1 - mRB\,\dot{\theta}_1\sin(\theta_c) = I_o\dot{\theta}_2 \quad (23)$$

where $\dot{\theta}_1$ is the angular velocity right before the impact and $\dot{\theta}_2$ is the angular velocity right after the impact. The ratio r of kinetic energy after and before each impact is expressed as:

$$r = \left(\dot{\theta}_2/\dot{\theta}_1\right)^2 = \left[1 - \frac{mRB}{I_o}\left(\sin(\theta_c)\right)\right]^2 = e^2 \quad (24)$$

where B is the short base for a trapezoidal block or the base for a rectangular block. The expression between brackets is referred to as the coefficient of restitution e, $(r = e^2)$. After performing some manipulations, Equation 24 can be simplified as (Makris and Roussos, 2000):

$$\ddot{\theta} + p^2\sin(\theta_c\text{sign}[\theta] - \theta) + p^2\sin(\theta_c\text{sign}[\theta] - \theta)\left(\frac{a_{yg}}{g}\right) = -p^2\cos(\theta_c\text{sign}[\theta] - \theta)\left(\frac{a_{xg}}{g}\right) \quad (25)$$

where $p = \sqrt{mgR/I_o}$ is the frequency parameter of the block in (rad/s). Equation 25 is solved via state-space formulation, using a fourth-order Runge–Kutta method as a numerical integrator in MATLAB (2018) with a time step of 1/10,000 sec. In integrating Equation 25, the initial conditions for rocking given by either Equations 20 or 21, and the coefficient of restitution e in Equation 24 need to be considered.

2D toppling model validation

To validate the 2D toppling model, first, two numerical examples accessible in the literature are reproduced. Second, the proposed toppling model is compared to the experimental results obtained from the CPT and accelerometers. The rotation and angular velocity time histories of a free-standing and base-isolated rigid block subjected to the Jensen Filter Plant motion, shown in Figure 13, exhibit an excellent agreement with the results presented by Vassiliou and Makris (2012). Similarly, the rotation and velocity responses of an anchored and free-standing rigid block subjected to the Rinaldi station motion, shown in Figure 14, successfully matched with the results reported by Makris and Zhang (2001), using two slightly different scaling factors for the input ground motion.

Locked patient stretcher PS2. Figure 15a (top) shows the building floor acceleration responses of the fifth level in the longitudinal (X) and transversal (Y) direction, respectively, when subjected to the FB-4: ICA100 motion. The second, third, and fourth rows of Figure 15a
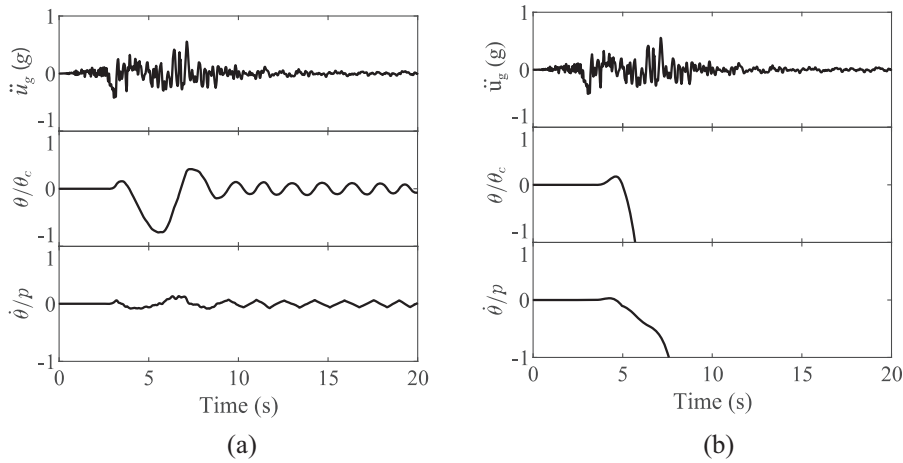
Figure 13. Rotation and angular velocity responses of a rigid block (b = 1.52 m, h = 10.33 m) subjected to the 022 component of the Jensen Filter Plant motion (PEER RSN983) (a) free-standing on a rigid foundation (no toppling) and (b) free-standing on an isolated base (T_b = 3 s, ξ = 0.1), right toppling.
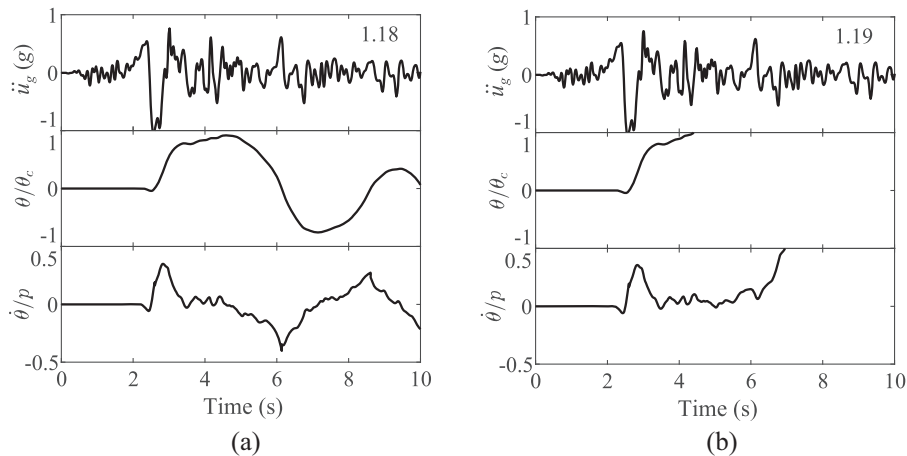

Figure 14. Rotation and angular velocity responses of an anchored rigid block (b = 2.0 m, h = 6.0 m, F_u/W = 0.4 and μ = 5) subjected to the 228 component of the Rinaldi Station motion (PEER RSN1063) (a) no toppling for PGA scaled up by 1.18 and (b) left toppling free-standing block for PGA scaled up by 1.19.

show the X, Y, and Z experimental displacement responses of the locked stretcher PS2 obtained from the CPT, respectively.

The predicted vertical displacements (gray dashed line), shown in Figure 15a (bottom), closely match the observed response (black solid line) obtained from the CPT. It is noteworthy to mention that the analytical model successfully predicted the toppling phenomenon, the toppling time, and the side on which the stretcher topples (right side in this case). The slight displacement ($\approx$1 cm) of the stretcher in the Y-direction indicates that a small slip occurs before toppling.

It should be recalled that the 2D analytical model is not capable of predicting the out-of-plane slip due to the initial assumptions made. However, and particularly for this case,
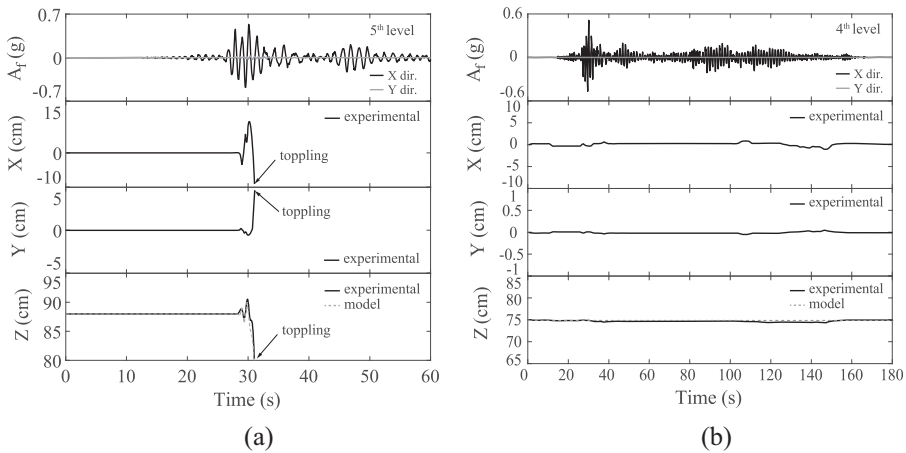
Figure 15. Experimental and analytical displacement and rotations responses of (a) stretcher PS2 (right toppling) and (b) patient bed PB1 (no toppling) subjected to the FB-4: ICA100 motion.

this slip is deemed to be negligible due to its magnitude, and because it neither influences the toppling nor the side on which the stretcher topples. Consequently, it is reasonable to assume that the 2D toppling model is valid until the FB-4: ICA100 motion since during the last two (strongest) FB motions it was observed that this stretcher experienced larger slips, along with lateral impacts from the rolling stretcher PS1.

Locked patient bed PB1. Figure 15b (top) displays the building floor acceleration responses of the fourth level when subjected to the FB-4: ICA100 motion. Figure 15b shows the X, Y, and Z displacement responses of the locked patient bed PB1 obtained from the CPT. Again, the results obtained from the numerical model show a close match with those obtained from experimentation. In this case, this bed did not topple due to its considerable high toppling angle ($\sim 16°$).

Figures 16a and 16b show the experimental acceleration responses of the locked stretcher PS2 when subjected to the FB-4 and FB-5 motions, respectively. These accelerations were recorded by the accelerometer installed at the mattress level. The toppling phenomenon observed in these figures can be interpreted by noticing the following events: (1) the accelerometer installed on top was first recording horizontal equipment accelerations in the longitudinal (E-W) direction of the building, then, (2) a considerable spike appeared in the acceleration trace, indicating that the equipment toppled and hit the floor, and (3) if the accelerometer was still functioning after toppling, it must have started recording vertical floor accelerations instead of horizontal accelerations due to the sudden 90° rotation of the stretcher.

Since the vertical floor accelerations of the UCSD building were approximately 1/10 of the horizontal accelerations (Pantoli et al., 2013a), the recording acceleration amplitudes obtained after toppling must be significantly lower than those before toppling. This sequence of events is clearly shown in both graphs. As can be seen, the locked stretcher PS2 topples at $t = 30.9$ sec. For the FB-4 motion. This confirms the responses captured by the CPT and those obtained from the analytical model (Figure 15a). Table 5 in Appendix 1 presents the model parameters used in the toppling models.
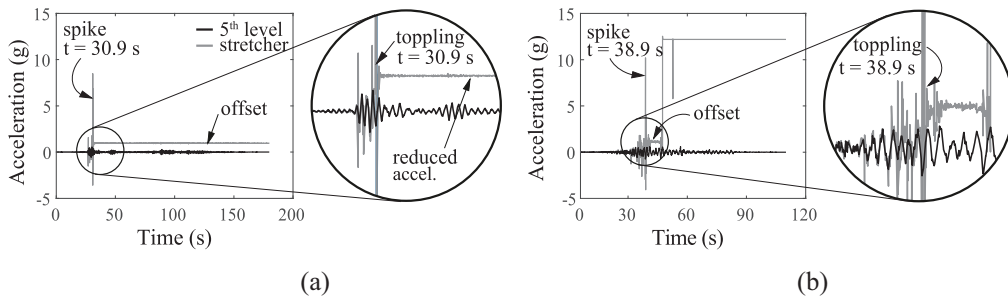
Figure 16. Experimental acceleration responses, toppling identification, and toppling times of locked stretcher PS2 subjected to (a) FB-4: ICA100 and (b) FB-5: DEN67 motions.

Wire shelving unit WSU1. The location of the video cameras MED5, and SI2 (shown in Figure 4b), along with the complex movement of several pieces of equipment made particularly difficult to use the CPT to adequately extract the sliding–rocking–toppling behavior of wire shelving unit WSU1. However, an insightful characterization of its behavior can be described as follows: (1) during the FB-4: ICA100 motion, this equipment was set into rocking motion, and then lost part of its inertial mass (water bottles) as indicated in Figure 17a; (2) during the FB-5: DEN67 motion, it fell over and got stuck on the rolling stretcher PS1, which added an eccentric inertial mass to the stretcher PS1 as shown in Figure 17b; and (3) during the FB-6: DEN100 motion, as shown in Figure 17c, this equipment completely toppled on the floor.

Figure 18 shows the acceleration responses of the WSU1 registered by an accelerometer located at the top level. These accelerations appear more jagged than those of the PS2, maybe due to its lightweight, and the significant changes in its inertial mass (Figure 17). Consequently, due to this convoluted behavior, the simulation of the WSU1 has not been included here. Based on the complex behavior observed during the last two (strongest) FB motions, more sophisticated numerical models would be necessary to simulate severe impacts, inertial mass variations, and flexibility of the equipment. Unfortunately, in this study, the equipment flexibility has not been accounted for due to the accelerometers did not record all horizontal responses, which are needed to validate their dynamic properties and frequencies. Moreover, detailed information on medical equipment components is not readily available.

Conclusions

The dynamic behavior of the medical equipment located at the fourth and fifth levels of the full-scale, five-story concrete building tested at the UCSD in 2012 was investigated. The medical equipment is comprised of the following unlocked wheeled equipment: (1) stretcher PS1, (2) patient bed PB2, (3) mobile metal cart MC2, and (4) ultrasound imager UI3; and the following locked/free-standing equipment: (1) stretcher PS2, (2) patient bed PB1, and (3) wire shelving unit WSU1. Based on the camera videos, it was found that the unlocked wheeled equipment exhibited rigid body motion and freely rolled on the floor, whereas the locked/free-standing equipment displayed vibration and rocking motion during the system identification tests. In addition, the equipment having rocking behavior experienced a smaller frequency variation than the equipment having rolling behavior.
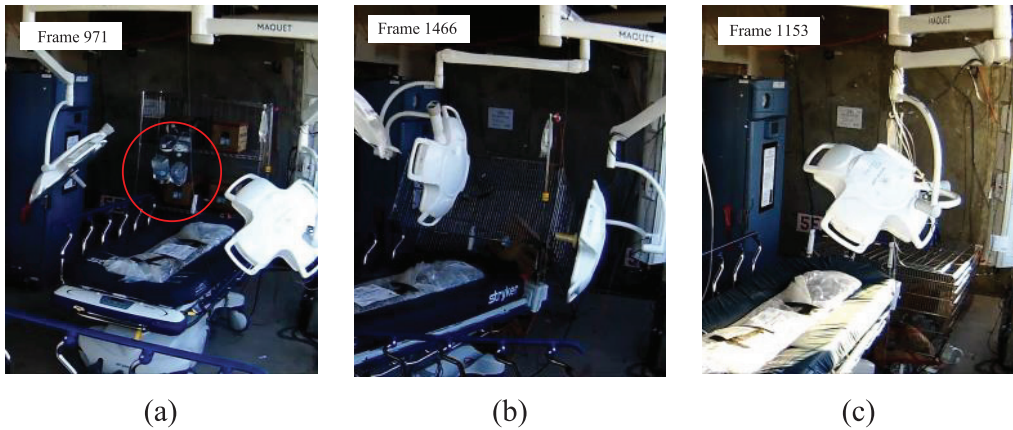
Figure 17. Damage scenes of the wire shelving unit WSU1 subjected to: (a) FB-4: LAC100, (b) FB-5: DEN67, and (c) FB-6: DEN100 motions.
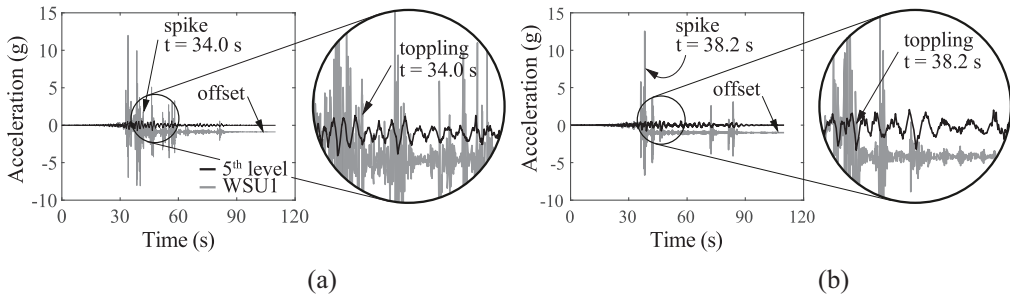

Figure 18. Experimental acceleration responses, toppling identification, and toppling times of wire shelving unit WSU1 subjected to: (a) FB-5: DEN67 and (b) FB-6: DEN100 motions.

Two nonlinear numerical models, namely, rolling and toppling, were developed to reproduce the experimental results obtained from the Camera Projection Technique (CPT). CPT was found to be reliable and capable of disclosing not only the equipment's horizontal displacements and rotations but also the rocking and toppling responses. The Euler–Lagrange formulation, along with the Stribeck friction model, was used to simulate the rolling, and in-plane rotation behavior of a four-wheel mobile cart (4WMC), which was considered to represent the dynamic trajectory of rolling equipment supported by swivel caster wheels. The 4WMC model was validated against the CPT experimental responses, and it was found that it closely matched not only the displacements, and in-plane rotations, but also the wheel steering angles. In addition, the numerical model was capable of exposing the pivot steering effect, as it certainly happened to MC2. It should be noted, however, that this numerical model does not consider lateral impacts, which indeed occurred during the last two (strongest) FB motions.

In addition, a simple 2D toppling model was used to describe the rocking–toppling behavior of locked and free-standing equipment. This numerical model was first, analytically validated by reproducing the results of two different numerical examples available in the literature, and second, it was compared to the experimental CPT and accelerometer responses. It was found that the numerical model faithfully reproduced both the analytical

and the experimental responses for PS2 and PB2. However, the simulation of the WSU1 was not feasible because of the camera positioning during the tests, and due to the complex equipment behavior observed during the last two (strongest) FB motions. Consequently, both the 4WMC and 2D toppling models successfully reproduced the equipment rolling, rocking, and toppling experimental responses as long as neither severe lateral impacts nor significant inertial mass variations occur during the motions. Finally, more sophisticated models would be required to adequately simulate severe lateral impacts, inertial mass variations, and flexibility of the equipment.

Acknowledgments

Declaration of conflicting interests

Funding

ORCID iD

Jaime Guamán-Cabrera https://orcid.org/0000-0002-7243-1534

References

American Society of Civil Engineers (ASCE) (2016) *Minimum Design Loads and Associated Criteria for Buildings and Other Structures* (ASCE/SEI 7-16). Reston, VA: ASCE.

American Society of Civil Engineers (ASCE) (2022) *Minimum Design Loads and Associated Criteria for Buildings and Other Structures* (ASCE/SEI 7-22). Reston, VA: ASCE.

Aslam M, Godden WG and Scalise DT (1978) Earthquake rocking response of rigid bodies. *Journal of the Structural Division: ASCE* 106(2): 377–392.

Bao Y and Konstantinidis D (2020) Dynamics of a sliding-rocking block considering impact with an adjacent wall. *Earthquake Engineering & Structural Dynamics* 49(5): 498–523.

Chatzis MN and Smyth AW (2012) Robust modeling of the rocking problem. *Journal of Engineering Mechanics: ASCE* 138(3): 247–262.

Chaudhuri S and Hutchinson T (2005) *Performance Characterization of Bench- and Shelf-Mounted Equipment*. Berkeley, CA: Pacific Earthquake Engineering Research Center (PEER), University of California, Berkeley.

Chen M, Pantoli E, Wang X, Astroza R, Ebrahimian H, Mintz S, Hutchinson T, Conte J, Restrepo J, Meacham B, Kim J and Park H (2013a) *BNCS Report #1: Full-Scale Structural and Nonstructural Building System Performance during Earthquakes and Post—Earthquake Fire—Specimen Design, Construction, and Test Protocol*. San Diego, CA: Department of Structural Engineering, University of California, San Diego.

Chen M, Pantoli E, Wang X, Mintz S, Hutchinson T and Restrepo J (2013b) *BNCS Report #4: Full-Scale Structural and Nonstructural Building System Performance during Earthquakes and Post—Earthquake Fire—Construction Details and Technical Specifications of Specific Subsystems.* San Diego, CA: Department of Structural Engineering, University of California, San Diego.

Chen MC, Pantoli E, Wang X, Astroza R, Ebrahimian H, Hutchinson TC, Conte JP, Restrepo JI, Marin C, Walsh KD, Bachman RE, Hoehler MS, Englekirk R and Faghihi M (2016) Full-scale structural and nonstructural building system performance during earthquakes: Part I—Specimen description, test protocol, and structural response. *Earthquake Spectra* 32: 737–770.

Cosenza E, Di Sarno L, Maddaloni G, Magliulo G, Petrone C and Prota A (2015) Shake table tests for the seismic fragility evaluation of hospital rooms. *Earthquake Engineering & Structural Dynamics* 44(1): 23–40.

D'Angela D, Magliulo G and Cosenza E (2021) Seismic damage assessment of unanchored nonstructural components taking into account the building response. *Structural Safety* 93: 102126.

Dhaouadi R and Hatab AA (2013) Dynamic modelling of differential-drive mobile robots using Lagrange and Newton-Euler methodologies: A unified framework. *Advances in Robotics & Automation* 2(2): 1000107.

Di Sarno L, Magliulo G, D'Angela D and Cosenza E (2019) Experimental assessment of the seismic performance of hospital cabinets using shake table testing. *Earthquake Engineering & Structural Dynamics* 48(1): 103–123.

Di Sarno L, Petrone C, Magliulo G and Manfredi G (2015) Dynamic properties of typical consultation room medical components. *Engineering Structures* 100: 442–454.

ElGawady MA, Ma Q, Butterworth JW and Ingham J (2011) Effects of interface material on the performance of free rocking blocks. *Earthquake Engineering & Structural Dynamics* 40(4): 375–392.

Faugeras O (1993) *Three-Dimensional Computer Vision: A Geometric Viewpoint.* Cambridge, MA: MIT Press.

Fragiadakis M and Diamantopoulos S (2020) Fragility and risk assessment of freestanding building contents. *Earthquake Engineering & Structural Dynamics* 49(10): 1028–1048.

Giresini L, Fragiacomo M and Sassu M (2016) Rocking analysis of masonry walls interacting with roofs. *Engineering Structures* 116: 107–120.

Guzman Pujols JC and Ryan KL (2016) Development of generalized fragility functions for seismically induced content disruption. *Earthquake Spectra* 32(3): 1303–1324.

Hang P and Chen X (2021) Towards autonomous driving: Review and perspectives on configuration and control of four-wheel independent drive/steering electric vehicles. *Actuators* 10(8): 184.

Hanson W (2009) *Procedures in Critical Care.* New York: McGraw Hill.

Hartley R and Zisserman A (2004) *Multiple View Geometry in Computer Vision.* 2nd ed. Cambridge: Cambridge University Press.

Housner GW (1963) The behavior of inverted pendulum structures during earthquakes. *Bulletin of the Seismological Society of America* 53(2): 403–417.

Hutchinson T, Restrepo J, Conte J, Pantoli E, Chen M, Wang X, Astroza R and Ebrahimian H (2012) *Shake Table Testing of a Five Story Building Outfitted with NCSs (BNCS Project).* San Diego, CA: DesignSafe-CI.

Konstantinidis D and Makris N (2008) Experimental and analytical studies on the response of freestanding laboratory equipment to earthquake shaking. *Earthquake Engineering & Structural Dynamics* 38(6): 827–848.

Lee M-H and Li T-HS (2015) Kinematics, dynamics and control design of 4WIS4WID mobile robots. *The Journal of Engineering* 2015(1): 6–16.

Lupoi A, Cavalieri F and Franchin P (2014) Component fragilities and system performance of health care facilities. In: Pitilakis K, Crowley H and Kaynia AM (eds) *SYNER-G: Typology Definition and Fragility Functions for Physical Elements at Seismic Risk.* Cham: Springer, pp. 357–384.

Makris N and Roussos YS (2000) Rocking response of rigid blocks under near-source ground motions. *Géotechnique* 50(3): 243–262.

Makris N and Zhang J (2001) Rocking response of anchored blocks under pulse-type motions. *Journal of Engineering Mechanics: ASCE* 127(5): 484–493.

MATLAB (2018) *MATLAB version 9.4.0 (R2018a)*. Natick, MA: The MathWorks, Inc.

Myrtle RC, Masri SF, Nigbor RL and Caffrey JP (2005) Classification and prioritization of essential systems in hospitals under extreme events. *Earthquake Spectra* 21(3): 779–802.

National Institute of Standards and Technology (NIST) (2017) *Seismic Analysis, Design, and Installation of Nonstructural Components and Systems-Background and Recommendations for Future Work* (NIST GCR 17-917-44). Gaithersburg, MD: NIST.

Nikfar F and Konstantinidis D (2017a) Effect of the stick-slip phenomenon on the sliding response of objects subjected to pulse excitation. *Journal of Engineering Mechanics: ASCE* 143(4): 04016122.

Nikfar F and Konstantinidis D (2017b) Evaluation of vision-based measurements for shake-table testing of nonstructural components. *Journal of Computing in Civil Engineering* 31(2): 04016050.

Nikfar F and Konstantinidis D (2017c) Shake table investigation on the seismic performance of hospital equipment supported on wheels/casters. *Earthquake Engineering & Structural Dynamics* 46(2): 243–266.

Nikfar F and Konstantinidis D (2019) Experimental study on the seismic response of equipment on wheels and casters in base-isolated hospitals. *Journal of Structural Engineering: ASCE* 145(3): 04019001.

Palmeri A and Makris N (2008) Response analysis of rigid structures rocking on viscoelastic foundation. *Earthquake Engineering & Structural Dynamics* 37(7): 1039–1063.

Pantoli E, Chen M, Wang X, Astroza R, Ebrahimian H, Mintz S, Hutchinson T, Conte J and Restrepo J (2013a) *BNCS Report #2: Full-Scale Structural and Nonstructural Building System Performance during Earthquakes and Post—Earthquake Fire—Test Results*. San Diego, CA: Department of Structural Engineering, University of California, San Diego.

Pantoli E, Chen M, Hutchinson T and Restrepo J (2013b) *BNCS Report #3: Full-Scale Structural and Nonstructural Building System Performance during Earthquakes and Post—Earthquake Fire—Camera and Analog Sensor Details*. San Diego, CA: Department of Structural Engineering, University of California, San Diego.

Perry J (1881) Notes on the rocking of a column. *Transactions of the Seismological Society of Japan* 3(1): 103–106.

Petrone C, Di Sarno L, Magliulo G and Cosenza E (2017) Numerical modelling and fragility assessment of typical freestanding building contents. *Bulletin of Earthquake Engineering* 15: 1609–1633.

Sato E, Furukawa S, Kakehi A and Nakashima M (2011) Full-scale shaking table test for examination of safety and functionality of base-isolated medical facilities. *Earthquake Engineering & Structural Dynamics* 40(13): 1435–1453.

Shenton HW III and Jones NP (1991) Base excitation of rigid bodies. I: Formulation. *Journal of Engineering Mechanics: ASCE* 117(10): 2286–2306.

Simchen E, Sprung CL, Galai N, Zitser-Gurevich Y, Bar-Lavi Y, Gurman G, Klein M, Lev A, Levi L, Zveibil F, Mandel M and Mnatzaganian G (2004) Survival of critically ill patients hospitalized in and out of intensive care units under paucity of intensive care unit beds. *Critical Care Medicine* 32(8): 1654–1661.

Szeliski R (2022) *Computer Vision: Algorithms and Applications*. London: Springer Nature.

Taghavi S and Miranda E (2003) *Response Assessment of Nonstructural Building Elements*. Berkeley, CA: Pacific Earthquake Engineering Research Center (PEER), University of California, Berkeley.

Vassiliou MF and Makris N (2012) Analysis of the rocking response of rigid blocks standing free on a seismically isolated base. *Earthquake Engineering & Structural Dynamics* 41: 177–196.

Wittich CE (2016) *Seismic response of freestanding structural systems: Shake table tests and model validation* (ProQuest Id: Wittich_ucsd_0033D_15947). Doctoral Dissertation, University of California, San Diego, San Diego, CA.

Wolff E and Constantinou M (2004) *Experimental Study of Seismic Isolation Systems with Emphasis on Secondary System Response and Verification of Accuracy of Dynamic Response History*

Analysis Methods. Buffalo, NY: Department of Civil, Structural and Environmental Engineering, University at Buffalo.

Xia F (2003) Modelling of a two-dimensional Coulomb friction oscillator. *Journal of Sound and Vibration* 265(5): 1063–1074.

Yim C-S, Chopra AK and Penzien J (1980) Rocking response of rigid blocks to earthquakes. *Earthquake Engineering & Structural Dynamics* 8(6): 565–587.

Yu P, Zhai C, Liu J and Wang X (2023) Shake table tests for the seismic performance assessment of desktop medical laboratory equipment considering the effect of adjacent walls and restrainers. *Structures* 50: 1922–1933.

Appendix 1

Table 1. List of earthquake motion tests conducted in the base-isolated and fixed-base systems

Name	Earthquake event-site scaling (%)	PIA[a] (g)	PIV[a] (cm/s)	PID[a] (cm)
BI-1: CNP100	1994 Northridge-Canoga Park (100)	0.21	23.37	8.42
BI-2: LAC100	1994 Northridge-LA City Terrace (100)	0.25	24.48	8.95
BI-3: SP100	2010 Maule (Chile)-San Pedro (100)	0.52	34.87	8.27
BI-4: ICA50	2007 Pisco (Peru)-Ica (50)	0.17	22.32	4.76
BI-5: ICA100	2007 Pisco (Peru)-Ica (100)	0.32	42.59	9.46
BI-6: ICA140	2007 Pisco (Peru)-Ica (140)	0.50	62.59	12.92
FB-1: CNP100	1994 Northridge-Canoga Park (100)	0.21	23.50	8.78
FB-2: LAC100	1994 Northridge-LA City Terrace (100)	0.18	23.05	9.31
FB-3: ICA50	2007 Pisco (Peru)-Ica (50)	0.21	26.22	5.83
FB-4: ICA100	2007 Pisco (Peru)-Ica (100)	0.26	28.49	7.32
FB-5: DEN67	2002 Denali-TAPS Pump St. #9 (67)	0.64	63.74	20.06
FB-6: DEN100	2002 Denali-TAPS Pump St. #9 (100)	0.80	83.57	33.62

[a]Achieved peak input acceleration (PIA), velocity (PIV), and displacement (PID) on the shake table.

Table 2. Support conditions, external dimensions, and weight of medical equipment investigated

Level	Equipment	Support condition	Width (m)	Length (m)	Height (m)	Weight (kg)
Fourth	UI3	Unlocked	0.55	0.70	1.47	180
	MC2	Unlocked	0.90	0.65	2.03	118
	PB1	Locked	1.05	2.36	0.76	259
	PB2	Unlocked	1.05	2.36	0.76	259
Fifth	PS1	Unlocked	1.00	2.20	0.76	150
	PS2	Locked	1.00	2.20	0.76	150
	WSU1	Free standing	0.66	1.22	1.88	43.6

Table 3. Identified fundamental frequencies of medical equipment located on the fourth and fifth stories

Test description	Fundamental frequencies (Hz)						
	PS2	PB1	WSU1	UI3	PS1	MC2	PB2
Double pulse and white noise before FB-1[a]	2.90	3.10	3.20	3.90	3.26	3.50	3.60
White noise before FB-6[b]	2.70	2.90	3.00	3.03	3.62	2.70	2.40

[a]Corresponds to the floor excitation at fourth or fifth floor level (7 May 2012).
[b]Corresponds to the floor excitation at fourth or fifth floor level (15 May 2012).

Table 4. Parameters used in the four-wheel mobile cart (4WMC) model

Description	Symbol	Unit	Stretcher PS1	Patient bed PB2	Mobile cart MC2	Ultrasound UI3
Platform length	$2a$	m	2.20	2.36	0.65	0.70
Platform width	$2b$	m	1.00	1.05	0.90	0.55
Platform mass[a]	m_p	kg	234	350	154	180
Platform, initial rotation angle	θ	degree	≈ 6	≈ 8	≈ 15	≈ 0
Wheel diameter	d_w	m	0.20	0.20	0.125	0.15
Wheel width	e_w	m	0.045	0.055	0.030	0.030
Wheel mass	m_w	kg	1.00	1.50	0.50	0.50
Wheel 1, initial steering angle	δ_1	degree	≈ 80	−35	0	0
Wheel 2, initial steering angle	δ_2	degree	0	0	0	0
Wheel 3, initial steering angle	δ_3	degree	0	0	0	0
Wheel 4, initial steering angle	δ_4	degree	≈ 80	35	0	0
Static rolling friction coefficient	$\mu_{s\varphi}$	–	0.045	0.012	0.044	0.025
Static rotational friction coefficient	$\mu_{s\delta}$	–	0.00049	0.00132	0.044	0.001
Kinetic rolling friction coefficient	$\mu_{k\varphi}$	–	0.00049	6.0e-4	0.0044	0.001
Kinetic rotational friction coefficient	$\mu_{k\delta}$	–	2.45e–05	1.2e–4	0.0044	5.00e–5
Transition sharpness parameter	β	s/m	19.76	15.00	6.05	0.49
Viscous damping constant	γ_n	–	0.0014	0.00042	0.00044	0.0001
Velocity exponent	p	–	1	1	1	1

[a]Includes extra weight added before tests.

Table 5. Trapezoidal and rectangular rigid block dimensions for modeling rocking equipment

Equipment	Trapezoidal block			Rectangular block		
	B_1 (m)	B_2 (m)	H (m)	B (m)	H (m)	f (%)
PB1	0.705	1.335	1.500	0.705	1.500	5.26
PS2	0.349	1.082	1.082	0.349	1.082	8.50